

Sum-Rate Maximization of RIS-Aided Digital and Holographic Beamformers in MU-MISO Systems

Pavan Kumar Gadamsetty*, K. V. S. Hari* and Lajos Hanzo†

*Department of Electrical Communication Engineering, Indian Institute of Science, Bengaluru 560012, India

†School of Electronics and Computer Science, University of Southampton, SO17 1BJ Southampton, U.K.

Abstract—Reconfigurable holographic surfaces (RHS) are intrinsically amalgamated with reconfigurable intelligent surfaces (RIS), for beneficially ameliorating the signal propagation environment. This potent architecture significantly improves the system performance in non-line-of-sight scenarios at a low power consumption. Briefly, the RHS technology integrates ultra-thin, lightweight antennas onto the transceiver, for creating sharp, high-gain directional beams. We formulate a user sum-rate maximization problem for our RHS-RIS-based hybrid beamformer. Explicitly, we jointly design the digital, holographic, and passive beamformers for maximizing the sum-rate of all user equipment (UE). To tackle the resultant nonconvex optimization problem, we propose an alternating maximization (AM) framework for decoupling and iteratively solving the subproblems involved. Specifically, we employ the zero-forcing criterion for the digital beamformer, leverage fractional programming to determine the radiation amplitudes of the RHS and utilize the Riemannian conjugate gradient algorithm for optimizing the RIS phase shift matrix of the passive beamformer. Our simulation results demonstrate that the proposed RHS-RIS-based hybrid beamformer outperforms its conventional counterpart operating without an RIS in multi-UE scenarios. The sum-rate improvement attained ranges from 8 bps/Hz to 13 bps/Hz for various transmit powers at the base station (BS) and at the UEs, which is significant.

Index Terms—Reconfigurable holographic surfaces (RHS), reconfigurable intelligent surfaces (RIS), beamforming, sum-rate, alternating maximization (AM).

I. INTRODUCTION

The next-generation wireless communication systems primarily aim for enhancing the reliable data transfer speeds, for reduced latency, and for providing ubiquitous connectivity [1], [2]. In particular, the millimeter-wave (mmWave) band, has emerged as one of the leading candidates for spectrum exploitation to address the impending spectrum scarcity and to facilitate high-speed data delivery. This mmWave band presents clear advantages owing to the rapid advances in its sophisticated circuit design [3]. In conjunction with the existing mmWave [4]–[6] bands, reconfigurable intelligent surfaces (RIS) have been proposed for enhancing the performance of future wireless systems [7]–[9]. Briefly, a RIS consists of a metasurface having programmable reflecting elements (PREs) that passively manipulate the incident waves, directing them towards desired destinations, unlike traditional signal relaying methods [10]. Thus, RIS address the limitations of conventional wireless channels by harnessing the unique capability of metasurfaces to manipulate the electromagnetic waves [11]. This manipulation enables various applications,

including arbitrary aperture beamforming [11], polarization conversion [12], and beam focusing [13].

Wireless signals in the mmWave bands experience significant path loss, resulting in potential performance degradation. To address this issue in mmWave systems, it is essential to jointly design the active beamformer at the base station (BS) and the passive beamformer at the RIS. As for the active beamformer at the BS, originally analog beamforming was proposed, which is based on a fully-connected (FC) architecture, where each radio frequency (RF) chain was connected to all antennas [14]. However, this approach required an excessive number of phase shifters, even for a low number of RF chains, leading to considerable power consumption. Hybrid beamforming (HBF) emerged as a practical low-power solution, combining analog and digital (baseband) beamformers, where each RF chain is connected to a subset of antennas [15].

Extensive research has been focused on the design of HBF, with multiple studies investigating the challenging aspects of this design [15], [22]–[27], including multiuser (MU) HBF [22], [27]. A predominant focus of MU beamforming is the maximization of sum-rate (SR). In [28], the authors proposed a joint design of PREs and MU beamforming in a narrow-band scenario to maximize the users' sum-rate. Additionally, weighted sum-rate (WSR) algorithms have been proposed in a Multiple-Input Single-Output (MISO) multiuser downlink scenario in [17], [18]. These algorithms jointly optimize beamforming at the BS and the phase coefficients of RIS elements to enhance the WSR. Furthermore, alternating optimization methods have been proposed for maximizing the achievable rate by jointly optimizing the transmit beamformer and the non-diagonal RIS phase shift matrix in [19], [20]. In the existing HBF techniques, phased arrays are used at the BS, with a RIS positioned between the BS and the user equipments (UEs) for preventing line-of-sight (LOS) blocking.

However, even when using phased arrays-based HBF in the mmWave band, the associated hardware costs and power consumption remain excessive, imposing a significant challenge [29]. This is because phased arrays require numerous phase shifters and power amplifiers to construct phase-shifting circuits for accurate beamforming. Additionally, as the operating frequency of massive multiple-input multiple-output (MIMO) systems increases, the implementation of phased arrays becomes prohibitive, severely hindering their future development. Therefore, there is an urgent need for developing bespoke technologies to meet the exponentially increasing data demands in next-generation wireless communications.

TABLE I: COMPARING OUR CONTRIBUTION TO THE EXISTING LITERATURE

	[16]	[17]	[18]	[19]	[20]	[21]	[22]	[23]	Proposed
mmWave channel	✓		✓		✓	✓	✓	✓	✓
Multi-UE		✓	✓	✓	✓	✓	✓	✓	✓
Optimal power allocation		✓	✓	✓	✓	✓	✓		✓
Fractional programming		✓						✓	✓
Manifold optimization	✓	✓							✓
RIS		✓	✓	✓	✓				✓
Holographic beamformer						✓			✓
Sum-rate		✓	✓		✓	✓		✓	✓
Dinkelbach-based method									✓
RHS-RIS combination									✓
Mutual coupling at RHS									✓

In contrast to RIS, the reconfigurable holographic surfaces (RHS) are capable of addressing the limitations of existing antenna technologies [21], [30]–[32], such as conventional phased array architectures. RHS, proposed as a representative metamaterial antenna [33], leverages the holographic interference principle to control the radiation amplitude of incoming electromagnetic waves. For supporting flexible beam steering, the RHS relies on a large number of metamaterial radiation elements connected to RF chains and it is generally integrated with the transceivers. This approach enables the creation of large arrays, while maintaining compact and lightweight transceiver hardware [34].

The physical structure of RHSs is different from that of the reconfigurable intelligent surfaces (RISs) [7]. Specifically, an RHS integrates its RF front end into a PCB, allowing for convenient transceiver implementation without requiring an extra control link to construct the holographic pattern. By contrast, an RIS places its RF front end on the outside in support of its reflective action, hence necessitating an additional control link between the RIS and the transmitter to adjust the phase shifts and/or radiation amplitudes. Because of these structural differences, RHSs typically serve as transmit and receive antennas, while RISs are commonly used as relays. Consequently, the active and passive beamforming design of RHSs and RISs are quite different.

For improving the system’s sum-rate, it is beneficial to simultaneously harness the advantages of both an RHS and RIS. This joint deployment is particularly useful in dense environments exhibiting blocked line-of-sight paths between BS and UEs. Passive RIS beamforming enhances the received signals, while RHS transmitters promptly adapt to fast-fading channels. Despite the challenge of jointly designing the passive and holographic beamformers, integrating an RHS and RIS significantly improves the signal quality, beamforming, energy efficiency, coverage, and cost-effectiveness. This potent combination promises to beneficially ameliorate the signal propagation, enhance coverage and increase the capacity, hence paving the way for advanced wireless communication networks.

The authors of [21] introduced the RHS in a mmWave system and solved a sum-rate maximization problem for RHS-based HBF in the absence of a RIS. However, even with

improved beam control, RHS-aided systems yielded poor performance in the absence of a stable line-of-sight link, thereby emphasizing the need to employ an RIS [35]. In [36], the authors exploit both RHS and RIS systems in the context of a Dual-function radar-communications (DFRC) system to maximize the radar signal-to-interference-plus-noise ratio (SINR), while ensuring the required communication SINR for all UEs. None of the existing works utilized both RHS and RIS technologies and solved the problem of obtaining the sum-rate expression for a mmWave multi-UE system.

Against the above background, this is the first piece of work maximizing the sum-rate through the joint optimization of digital, holographic, and passive beamformers. The resultant optimization problem is nonconvex along with coupled variables. To address this challenge, we decouple the problem into several subproblems, which are then solved using an alternating maximization (AM) algorithm [37]. Specifically, we employ zero-forcing beamforming [38] for the digital beamforming, utilize fractional programming [39] to determine the radiation amplitudes of the RHS elements, and leverage the Riemannian conjugate gradient algorithm [40] to obtain the optimal RIS phase shift matrix for the passive beamformer. Simulation results demonstrate the effectiveness of the proposed algorithm, exhibiting improvements over existing RHS-based methods operating without an RIS.

We summarize the main contributions of the paper as:

- 1) A RHS-RIS-aided MU mmWave MISO system model is developed, for supporting single-antenna UEs. The end-to-end channel gains are determined for this system, considering scenarios both with and without the RIS. Subsequently, a sum-rate maximization problem is formulated to determine the joint active and passive beamformers for the RIS system with the objective of maximizing the system’s sum-rate. Again, this optimization problem is non-convex.
- 2) We proposed an alternating maximization algorithm for HBF design, aiming for maximizing the sum-rate of the UEs. The front-end digital beamformer matrix is obtained via the zero-forcing technique, followed by optimal power allocation. The holographic beamforming subproblem is solved using fractional programming. The unit modulus constraints of the RIS phase shift matrix

define a Riemannian manifold, leading us to propose a manifold optimization-based algorithm.

- 3) Extensive simulations demonstrate the remarkable benefits of the proposed algorithm in terms of the signal-to-interference-plus-noise ratio (SINR) and the number of UEs in the system. The numerical results indicate a substantial sum-rate improvement.

The remainder of this paper is organized as follows. Section II presents the system model. In Section III, the proposed AM algorithm is discussed. The performance of the proposed algorithm is discussed in Section IV and we conclude in Section V.

Notation: Scalars are denoted by italic letters, lower (upper) case bold letters denote column vectors (matrices). The superscripts $(\cdot)^{-1}$, $(\cdot)^*$, $(\cdot)^H$ represent inverse, complex conjugate, and Hermitian operators, respectively. The symbol $\|\cdot\|_F$ denotes the Frobenius norm of a matrix, the \circ operator denotes the element-wise product, while \Re and \Im represent the real and imaginary part, respectively. For a matrix \mathbf{A} , $\mathbf{A}(i, i)$ represents the i -th diagonal element, and $\text{Tr}(\mathbf{A})$ denotes its trace. Furthermore, $\mathbf{A}_{i,j}$ denotes the element in the i -th row and the j -th column. For a vector \mathbf{a} , $\mathbf{a}(i)$ represents the i -th element, $\text{diag}(\mathbf{a})$ denotes the diagonal matrix whose diagonal elements are the corresponding elements in \mathbf{a} , and $\mathbf{1}_K$ is an all-one vector of dimension $K \times 1$.

II. SYSTEM MODEL

In this section, we will first present the system model and channel model of the mmWave MISO system considered. Then we formulate the RHS-RIS-aided HBF problem.¹

Consider the mmWave multi-UE MISO downlink (DL) scenario, as illustrated in Fig. 1. The system consists of a uniform planar array (UPA) having N_t RHS elements at the BS, an RIS featuring N_{RIS} elements, and K UEs having a single receive antenna (RA) each. The antennas at the BS (RIS) along the x - and y -axes are denoted as N_t^x (N_{RIS}^x) and N_t^y (N_{RIS}^y), respectively. The BS transmits K data streams, and each UE receives a single data stream from the BS. To enhance the beamforming capabilities, a RHS is employed at the BS, utilizing holographic techniques. The RHS is fed by N_{RF} radio-frequency (RF) chains, eliminating the need for phase-shifters.

Let $\mathbf{s} \in \mathbb{C}^{K \times 1}$ represent the transmitted symbol before beamforming at the BS, where $\mathbf{s} = [s_1, \dots, s_K]^T$, and s_k denotes the information signal of the k -th UE, for $k = 1, \dots, K$. The symbols s_k are assumed to be independent with an average power of one, i.e., $\mathbb{E}[\mathbf{s}\mathbf{s}^H] = \mathbf{I}_K$. The symbol vector \mathbf{s} is first precoded by the digital beamformer matrix $\mathbf{F} = [\mathbf{f}_1, \dots, \mathbf{f}_K] \in \mathbb{C}^{N_{RF} \times K}$ and subsequently passed through the RF chains to the RHS beamformer $\mathbf{M}_v \in \mathbb{C}^{N_t \times N_{RF}}$. The RIS is assumed to have a diagonal phase shift matrix $\mathbf{\Theta}_{RIS} = \text{diag}\{e^{j\theta_1}, \dots, e^{j\theta_{N_{RIS}}}\} \in \mathbb{C}^{N_{RIS} \times N_{RIS}}$ with N_{RIS} non-zero diagonal entries.

The matrices $\mathbf{H}_d = [\mathbf{h}_{d,1}, \dots, \mathbf{h}_{d,K}]^H \in \mathbb{C}^{K \times N_t}$, $\mathbf{H}_R = [\mathbf{h}_{R,1}, \dots, \mathbf{h}_{R,K}]^H \in \mathbb{C}^{K \times N_{RIS}}$ and $\mathbf{G}_R =$

$[\mathbf{g}_{R,1}, \dots, \mathbf{g}_{R,N_t}] \in \mathbb{C}^{N_{RIS} \times N_t}$ represent the direct channel spanning from the BS to K UEs, from the RIS to K UEs, and from the BS to RIS, respectively. Therefore, the effective channel emerging from the BS to the K UEs can be expressed as $\mathbf{H}_{tot} = \mathbf{H}_d + \mathbf{H}_R \mathbf{\Theta}_{RIS} \mathbf{G}_R$. In other words, we have $\mathbf{H}_{tot} = [\mathbf{h}_{tot,1}, \dots, \mathbf{h}_{tot,K}]^H$, where $\mathbf{h}_{tot,k}^H \in \mathbb{C}^{1 \times N_t}$ ($k = 1, 2, \dots, K$) represents the complete channel vector from the BS to the k -th single-antenna UE.

A. Channel model

A realistic channel model should account for both the large-scale fading and small-scale fading characteristics. However, the fading channel models commonly used in traditional MISO systems may not accurately represent the characteristics of mmWave channels. This discrepancy arises from the significant free-space path loss and the presence of large, closely-packed antenna arrays in mmWave environments. Therefore, to accurately capture the characteristics of mmWave propagation, the Saleh-Valenzuela channel model [4], [43] is utilized. The mmWave channel can be represented as

$$\mathbf{h}_{d,k}^H = \sqrt{\frac{N_t}{L_d}} \sum_{l_d=1}^{L_d} \alpha_{l_d} \mathbf{a}_r(\phi_{l_d}^r) \mathbf{a}_t(\phi_{l_d}^t, \varphi_{l_d}^t)^H, \quad (1)$$

$$\mathbf{h}_{R,k}^H = \sqrt{\frac{N_{RIS}}{L_{ru}}} \sum_{l_u=1}^{L_{ru}} \alpha_{l_u} \mathbf{a}_r(\phi_{l_u}^r) \mathbf{a}_t(\phi_{l_u}^t, \varphi_{l_u}^t)^H, \quad (2)$$

$$\mathbf{G}_R = \sqrt{\frac{N_{RIS} N_t}{L_{br}}} \sum_{l_b=1}^{L_{br}} \alpha_{l_b} \mathbf{a}_r(\phi_{l_b}^r, \varphi_{l_b}^r) \mathbf{a}_t(\phi_{l_b}^t, \varphi_{l_b}^t)^H, \quad (3)$$

where L_d , L_{ru} and L_{br} denote the number of multipath components in $\mathbf{h}_{d,k}$, $\mathbf{h}_{R,k}$, and \mathbf{G}_R , respectively. Let the first path in $\mathbf{h}_{R,k}$ and \mathbf{G}_R denote the line-of-sight components. Furthermore, α_{l_*} denotes the complex channel gain of the l_* -th path, while (ϕ_*^r, φ_*^r) and (ϕ_*^t, φ_*^t) refer to the physical angle of arrival and angle of departure, respectively. The vectors $\mathbf{a}_r(\phi_*^r, \varphi_*^r)$ and $\mathbf{a}_t(\phi_*^t, \varphi_*^t)$ represent the antenna array response vectors. It is assumed that each UE has a single receive antenna, and thus, we have $\mathbf{a}_r(\phi_{l_u}^r) = \mathbf{a}_r(\phi_{l_d}^r) = 1$. The array response vectors can be written as

$$\mathbf{a}_z(\phi, \varphi) = \sqrt{\frac{1}{N^x N^y}} \left[1, \dots, e^{j \frac{2\pi}{\lambda} d (n^x \sin \phi \sin \varphi + n^y \cos \varphi)}, \dots, e^{j \frac{2\pi}{\lambda} d ((N^x - 1) \sin \phi \sin \varphi + (N^y - 1) \cos \varphi)} \right]^T. \quad (4)$$

Here, $z \in \{r, t\}$ and, $0 \leq n^x \leq (N^x - 1)$ and $0 \leq n^y \leq (N^y - 1)$. The variables N^x and N^y represent the number of horizontal and vertical elements, respectively, of the UPA in the 2D plane. The inter-element spacing along the x - and y -axes for the UPA at the BS and the RIS is denoted by d , which is dependent on the wavelength λ . Additionally, $\phi \in [0, 2\pi]$ and $\varphi \in [0, \pi/2]$ represent the azimuth and elevation angles, respectively.

B. RHS Transmitter

The RHS lacks digital processing capability, requiring the BS to perform signal processing at the baseband. As shown

¹In this work we have considered switch-controlled RHS-aided beamforming architecture [21], [41], [42].

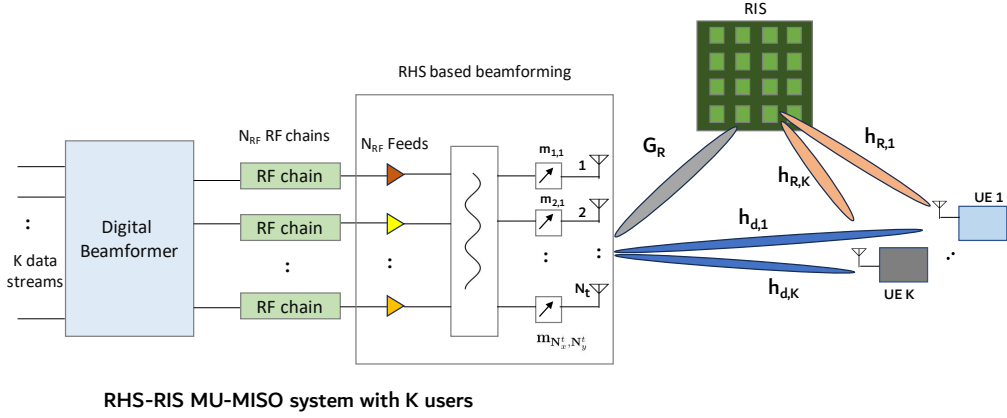


Fig. 1: Overview of the RHS-RIS MU-MISO system having K UEs with one receive antenna, a BS with N_t RHS elements and an RIS with N_{RIS} elements.

in Fig. 1, the BS encodes K distinct data streams using a digital beamformer matrix \mathbf{F} and subsequently up-converts the processed signals to the carrier frequency through RF chains. Each RF chain is linked to a feed on the RHS, aligning the number of RF chains with the number of feeds N_{RF} . Every RF chain transmits the up-converted signals to its connected feed. The feed then converts the high-frequency current into an electromagnetic wave (reference wave) propagating on the RHS. Since the feeds of the RHS directly connect with the RF chains, there is no channel or attenuation between the BS and the RHS [21]. To generate the desired beams, the radiation amplitude of the reference wave at each element is controlled by a holographic beamformer matrix \mathbf{M} .

The RHS has N_{RF} feeds and $(N_t^x \times N_t^y)$ discrete elements. The electromagnetic response is given by

$$\mathbf{M}_v = \mathbf{M}\mathbf{V} \in \mathbb{C}^{N_t^x N_t^y \times N_{RF}}, \quad (5)$$

where each element of the matrix \mathbf{V} is represented as $\mathbf{V}(p, q) = e^{-2\pi\gamma D_{p,q}/\lambda}$, where $D_{p,q}$ denotes the distance between the p -th RHS element and the q -th feed. The matrix $\mathbf{M} = \text{diag}[m_{1,1}, \dots, m_{1,N_t^y}, \dots, m_{N_t^x,1}, \dots, m_{N_t^x, N_t^y}]$ is a diagonal matrix, with amplitude-control beamformer values $0 \leq m_{x,y} \leq 1$ for each (x, y) -th RHS element.²

The dimensions of the holographic surface are represented by N_t^x and N_t^y . The parameter γ denotes the refractive index of the material on the RHS. Thus, when the structure of the holographic surface is fixed, the matrix \mathbf{V} is pre-determined.

1) *Holographic interference principle:* An RHS functions as a leaky-wave antenna comprising three layers, i.e., N_{RF} feeds connect with the corresponding RF chain embedded in the lowest layer. The waveguide structure in the middle layer guides the reference wave to the N_t discrete sub-wavelength metamaterial elements integrated on the top layer [44]. Specifically, at the (x, y) -th RHS element, the reference wave imported from the q -th feed and the desired wave propagating in the target direction (ϕ_0, φ_0) are characterized by the following

expressions, respectively:

$$\Psi_{obj}(\mathbf{r}_{x,y}, \phi_0, \varphi_0) = \exp(-j\mathbf{k}_f(\phi_0, \varphi_0) \cdot \mathbf{r}_{x,y}), \quad (6)$$

$$\Psi_{ref}(\mathbf{r}_{x,y}^q) = \exp(-j\mathbf{k}_r \cdot \mathbf{r}_{x,y}^q). \quad (7)$$

Here, \mathbf{k}_f represents the desired directional channel vector in free space, \mathbf{k}_r is the channel vector of the reference wave, $\mathbf{r}_{x,y}$ is the position vector of the (x, y) -th radiation element, and $\mathbf{r}_{x,y}^q$ is the distance vector of the link between the feed q and (x, y) -th radiation element. The interference between the reference wave and the desired object wave is defined as follows:

$$\Psi_{intf}(\mathbf{r}_{x,y}^q, \phi_0, \varphi_0) = \Psi_{obj}(\mathbf{r}_{x,y}, \phi_0, \varphi_0) \Psi_{ref}^*(\mathbf{r}_{x,y}^q). \quad (8)$$

The RHS can only generate the holographic pattern using the fixed reference wave given in (8). When the holographic pattern is excited by the reference wave, we have the following result:

$$\Psi_{intf}(\mathbf{r}_{x,y}^q, \phi_0, \varphi_0) \Psi_{ref}(\mathbf{r}_{x,y}^q) \propto \Psi_{obj}(\mathbf{r}_{x,y}, \phi_0, \varphi_0) |\Psi_{ref}(\mathbf{r}_{x,y}^q)|^2. \quad (9)$$

To generate the desired wave in the direction (ϕ_0, φ_0) we control the interference as described in (8). Furthermore, it is clear from the (8) and (9) that generating the interference waves requires phase adjustment. However, in contrast to conventional phased arrays, the elements of a RHS can only adjust the radiation amplitude of the reference wave. Each radiation element is electrically tuned to resonate at a specific frequency and to emit a reference wave. The specific elements whose emitted waves are aligned in phase with the desired directional beam (i.e., the sum of all radiation elements' waves) are tuned to emit strongly, while those that are out of phase are adjusted to radiate weakly or not at all [34]. The real part of the interference (i.e., $\text{Re}[\Psi_{intf}]$) represents the cosine of the phase difference between the object wave and the reference wave. As this phase difference increases, $\text{Re}[\Psi_{intf}]$ decreases, meeting the requirement for amplitude control. Thus, $\text{Re}[\Psi_{intf}]$ serves as a measure of the radiation amplitude for each radiation element. To ensure non-negative values, $\text{Re}[\Psi_{intf}]$ is normalized to a range of $[0, 1]$. The

²We use the terms BS antennas and RHS elements interchangeably.

radiation amplitude of each radiation element required for generating a wave propagating in the direction (ϕ_0, φ_0) can then be mathematically formulated as:"

$$m_{x,y}(r_{x,y}^q, \phi_0, \varphi_0) = \frac{\text{Re}[\Psi_{\text{intf}}(\mathbf{r}_{x,y}^q, \phi_0, \varphi_0)] + 1}{2}. \quad (10)$$

According to (10), it is observed that the particular elements whose reference waves closely match the object wave (i.e., have a large amplitude) are tuned to emit strongly. Conversely, the radiation elements that do not closely match are tuned down or even turned off. For the multi-beam design of the holographic pattern, the amplitude of each element is then determined accordingly as

$$m_{x,y}(r_{x,y}^q, \phi_0, \varphi_0) = \sum_{k=1}^K \sum_{q=1}^{N_{RF}} a_{k,q} m_{x,y}(r_{x,y}^q, \phi_k, \varphi_k) \quad \forall (x, y). \quad (11)$$

Here, $a_{k,q}$ denotes the amplitude ratio for the beam directed towards the k -th UE from the q -th feed, and it must satisfy the condition: $\sum_{k=1}^K \sum_{q=1}^{N_{RF}} a_{k,q} = 1$. This condition ensures that the total amplitude contribution across all directions and feeds sums to 1, which also ensures $0 \leq m_{x,y} \leq 1$.

C. Received Signal at the k -th UE

The intended signal vector for K UEs is $\mathbf{s} \in \mathbb{C}^{K \times 1}$. Consequently, the signals transmitted from the BS are expressed by the vector \mathbf{F} s. Therefore, the signal received by the k -th UE, denoted as y_k , can be expressed as follows:

$$\begin{aligned} y_k &= \mathbf{h}_{\text{tot},k}^H \mathbf{M}_v \mathbf{F} \mathbf{s} + n_k, \quad (12) \\ &= \underbrace{\mathbf{h}_{\text{tot},k}^H \mathbf{M}_v \mathbf{f}_k s_k}_{\text{Intended signal}} + \underbrace{\mathbf{h}_{\text{tot},k}^H \mathbf{M}_v \sum_{k' \neq k} \mathbf{f}_{k'} s_{k'}}_{\text{Interference}} + \underbrace{n_k}_{\text{Receiver noise}}, \quad (13) \end{aligned}$$

where $n_k \sim \mathcal{CN}(0, \sigma^2)$ denotes the additive white Gaussian noise (AWGN) at the k -th UE.

D. Mutual Coupling

Mutual coupling in wireless communication systems refers to the interaction between closely placed antennas in an array, where the electromagnetic fields generated by one antenna affect the performance of neighboring antennas [45], [46]. Let the effects of mutual coupling among RHS elements be fully captured by the coupling matrix \mathbf{C} , which generally depends on the positions and radiation power patterns of the antenna elements. If the mutual coupling effect is not considered, the coupling matrix \mathbf{C} is assumed to be an identity matrix ($\mathbf{I}_{N_t \times N_t}$). In the RHS transmitter model associated with N_t discrete elements, the electromagnetic response including mutual coupling is given by

$$\mathbf{M}_v = \mathbf{C} \mathbf{M}_v, \quad \begin{cases} \mathbf{C} = \mathbf{I} & \text{Without mutual coupling} \\ \mathbf{C} \neq \mathbf{I} & \text{With mutual coupling.} \end{cases} \quad (14)$$

With mutual coupling, the signal received by the k -th UE is given by

$$y_k = \mathbf{h}_{\text{tot},k}^H \mathbf{C} \mathbf{M}_v \mathbf{F} \mathbf{s} + n_k. \quad (15)$$

We consider the N_t RHS elements at the BS to be isotropic, with equal spacing between the successive elements [47]. The elements in the mutual coupling matrix \mathbf{C} are modeled according to [48], and the coupling matrix is given by

$$\mathbf{C} = \mathbf{D}^{-1/2}, \quad (16)$$

where the matrix $\mathbf{D} = \{c_{n',n}\}$ is an $N_t \times N_t$ matrix, and for the element positions $\{\mathbf{t}_n \mid n = 1, 2, \dots, N_t\}$, $c_{n',n}$ is given by

$$c_{n',n} = \text{sinc}(2\|\mathbf{t}_{n'} - \mathbf{t}_n\|_2/\lambda), \quad (17)$$

where $\|\mathbf{t}_{n'} - \mathbf{t}_n\|_2$ represents the distance between the RHS elements n' and n . It can be observed that for an antenna array having a given geometrical deployment, where all the RHS antenna elements are isotropic, the coupling matrix \mathbf{C} in (16) is deterministic and only has to be computed once, offline. This approach is based on coupling-agnostic transceiver designs, which may result in a loss of performance. The corresponding simulations, with and without the effects of mutual coupling, are presented in the simulation results section for the proposed and existing methods. For simplicity, the coupling matrix \mathbf{C} is assumed to be the identity matrix \mathbf{I} for the rest of the paper, as this does not affect the analysis.

E. Beamformer Design

The achievable rate of the k -th UE is given by

$$R_k = \log_2 \left(1 + \frac{|\mathbf{h}_{\text{tot},k}^H \mathbf{M}_v \mathbf{f}_k|^2}{\sigma^2 + \sum_{k' \neq k} |\mathbf{h}_{\text{tot},k}^H \mathbf{M}_v \mathbf{f}_{k'}|^2} \right). \quad (18)$$

Our objective is to maximize the achievable DL sum-rate through the optimization of the digital beamformer matrix \mathbf{F} , the holographic beamformer matrix \mathbf{M} , and the RIS phase shift matrix Θ_{RIS} . The optimization problem is formulated as follows:

$$\begin{aligned} \max_{\{\mathbf{F}, \mathbf{M}, \Theta_{RIS}\}} & \sum_{k=1}^K R_k \\ \text{s.t.} & \text{Tr}(\mathbf{M} \mathbf{V} \mathbf{F} \mathbf{F}^H \mathbf{V}^H \mathbf{M}^H) \leq P_T, \\ & 0 \leq m_{x,y} \leq 1, \quad \forall x, y, \\ & |\Theta_{RIS}(i, i)|^2 = 1, \quad \forall i \end{aligned} \quad (19)$$

where P_T represents the total transmit power available at the BS. The amplitudes $m_{x,y}$ of the holographic beamformer are constrained to a maximum value of 1. Additionally, the constraint on Θ_{RIS} specifies that the RIS elements reflect the impinging signal without any loss of energy. The problem described in (19) is non-convex due to the product of optimization variables. Therefore, we rely on the AM algorithm, where in each step, we solve a subproblem, which is convex.

III. ALTERNATING MAXIMIZATION ALGORITHM

In this section, we implement an AM algorithm [37] to address the sum-rate maximization problem of the RHS-RIS-aided multi-UE communication system. The considered joint optimization problem is tackled by decomposing it into three subproblems: the digital beamforming subproblem, the holographic beamforming subproblem, and the RIS phase shift

matrix optimization subproblem. In the AM approach, the fundamental concept involves decomposing the optimization variables into multiple blocks. Subsequently, each block is updated following specific rules, while keeping the remaining blocks fixed at their previous updated values.

A. Problem Decomposition

To address the optimization problem described in (19) and achieve the best sum-rate, we decouple the nonconvex optimization problem into three subproblems outlined below. We solve these subproblems sequentially to obtain the optimal values for \mathbf{F} , \mathbf{M} and Θ_{RIS} .

1) *Digital Beamforming*: Given the holographic beamformer matrix \mathbf{M} and the RIS phase shift matrix Θ_{RIS} , the digital beamforming subproblem can be formulated as

$$\mathcal{P}_1: \max_{\{\mathbf{F}\}} \sum_{k=1}^K R_k, \quad s.t. \text{Tr}(\mathbf{M}_v \mathbf{F} \mathbf{F}^H \mathbf{M}_v^H) \leq P_T. \quad (20)$$

2) *Holographic Beamforming*: Given the optimal digital beamformer matrix \mathbf{F} of \mathcal{P}_1 and the RIS phase shift matrix Θ_{RIS} , the subproblem can be formulated as

$$\mathcal{P}_2: \max_{\{\mathbf{M}\}} \sum_{k=1}^K R_k, \quad s.t. 0 \leq m_{x,y} \leq 1, \quad \forall x, y. \quad (21)$$

3) *RIS phase optimization*: Given the optimal digital beamformer matrix \mathbf{F} of \mathcal{P}_1 and the optimal holographic beamformer matrix \mathbf{M} of \mathcal{P}_2 , the RIS phase shift matrix design subproblem can be formulated as

$$\mathcal{P}_3: \max_{\{\Theta_{RIS}\}} \sum_{k=1}^K R_k, \quad s.t. |\Theta_{RIS}(i, i)|^2 = 1, \quad \forall i. \quad (22)$$

The AM algorithm iterates between \mathcal{P}_1 , \mathcal{P}_2 , and \mathcal{P}_3 to obtain the optimal values for \mathbf{F} , \mathbf{M} , and Θ_{RIS} .

B. Digital Beamformer Design (\mathcal{P}_1)

The digital beamforming subproblem, obtained by substituting R_k from (18) into \mathcal{P}_1 is presented as follows:

$$\mathcal{P}_1: \max_{\{\mathbf{F}\}} \sum_{k=1}^K \log \left(1 + \frac{|\mathbf{h}_{tot,k}^H \mathbf{M} \mathbf{V} \mathbf{f}_k|^2}{\sigma^2 + \sum_{k' \neq k} |\mathbf{h}_{tot,k}^H \mathbf{M} \mathbf{V} \mathbf{f}_{k'}|^2} \right), \quad s.t. \text{Tr}(\mathbf{M} \mathbf{V} \mathbf{F} \mathbf{F}^H \mathbf{M} \mathbf{V}^H) \leq P_T. \quad (23)$$

The problem \mathcal{P}_1 is a well-known one, typically addressed using zero-forcing beamforming. In [38], it has been demonstrated that zero-forcing beamforming can achieve near-optimal solutions at low complexity. Therefore, we opt for employing zero-forcing beamforming along with power allocation as the low-dimensional digital beamformer at the BS. This decision is motivated by the need to mitigate the inter-user interference. The digital beamformer matrix can be expressed as follows:

$$\mathbf{F} = \mathbf{Q}^H (\mathbf{Q} \mathbf{Q}^H)^{-1} \mathbf{P}^{\frac{1}{2}} = \tilde{\mathbf{F}} \mathbf{P}^{\frac{1}{2}}, \quad (24)$$

where $\mathbf{Q} = [\mathbf{V}^H \mathbf{M}^H \mathbf{h}_{tot,1}, \dots, \mathbf{V}^H \mathbf{M}^H \mathbf{h}_{tot,K}] \in \mathbb{C}^{K \times N_{RF}}$, $\mathbf{P} = \text{diag}(p_1, \dots, p_K)$ is a diagonal matrix, and p_k represents the power received at the k -th UE. Using (24) and by

leveraging the properties of zero-forcing beamforming, i.e., $\mathbf{h}_{tot,k}^H \mathbf{M} \mathbf{V} \mathbf{f}_k = \sqrt{p_k}$ and $\mathbf{h}_{tot,k}^H \mathbf{M} \mathbf{V} \mathbf{f}_{k'} = 0, \forall k' \neq k$, the digital beamforming subproblem may be simplified into a power allocation problem, as presented below:

$$\max_{\{p_k\}} \sum_{k=1}^K \log_2 \left(1 + \frac{p_k}{\sigma^2} \right), \quad s.t. \text{Tr} \left(\mathbf{P}^{\frac{1}{2}} \tilde{\mathbf{F}}^H \mathbf{V}^H \mathbf{M}^H \mathbf{M} \mathbf{V} \tilde{\mathbf{F}} \mathbf{P}^{\frac{1}{2}} \right) \leq P_T, \quad p_k \geq 0. \quad (25)$$

The optimal p_k^* can be obtained by the water-filling algorithm [49] as

$$p_k^* = \frac{1}{\mu_k} \max \left\{ \frac{1}{\epsilon} - \mu_k \sigma^2, 0 \right\}, \quad (26)$$

where μ_k is the k -th diagonal element of $\tilde{\mathbf{F}}^H \mathbf{V}^H \mathbf{M}^H \mathbf{M} \mathbf{V} \tilde{\mathbf{F}}$, and ϵ is a normalization factor satisfying $\sum_{k=1}^K \max \left\{ \frac{1}{\epsilon} - \mu_k \sigma^2, 0 \right\} = P_T$. By obtaining the p_k^* values from (26), we obtain the matrix \mathbf{P} , upon substituting the matrix \mathbf{P} into $\mathbf{F} = \tilde{\mathbf{F}} \mathbf{P}^{\frac{1}{2}}$, we can then derive the optimal digital beamformer matrix \mathbf{F} .

C. Holographic Beamformer Design (\mathcal{P}_2)

The optimization problem described in (19) differs from the traditional phase-controlled analog beamforming design. The objective function in \mathcal{P}_2 is nonconvex as it involves optimization variables in fractional form. Consequently, the existing algorithms like the semi-definite programming (SDP) [19] and the gradient ascent algorithm [50] are unable to handle this. To address this challenge, we employ fractional programming [39] based optimization, which solves the problem \mathcal{P}_2 as a series of optimization problems discussed in this section:

$$\mathcal{P}_2: \max_{\{\mathbf{M}\}} \sum_{k=1}^K \log \left(1 + \frac{|\mathbf{h}_{tot,k}^H \mathbf{M} \mathbf{V} \mathbf{f}_k|^2}{\sigma^2 + \sum_{k' \neq k} |\mathbf{h}_{tot,k}^H \mathbf{M} \mathbf{V} \mathbf{f}_{k'}|^2} \right), \quad s.t. 0 \leq m_{x,y} \leq 1, \quad \forall x, y, \quad (27)$$

$$\mathcal{P}_{2.1}: \max_{\{\mathbf{M}\}} \sum_{k=1}^K \left(\frac{|\mathbf{h}_{tot,k}^H \mathbf{M} \mathbf{V} \mathbf{f}_k|^2}{\sigma^2 + \sum_{k' \neq k} |\mathbf{h}_{tot,k}^H \mathbf{M} \mathbf{V} \mathbf{f}_{k'}|^2} \right), \quad s.t. 0 \leq m_{x,y} \leq 1, \quad \forall x, y. \quad (28)$$

The subproblem \mathcal{P}_2 is not convex. To address \mathcal{P}_2 , we approximate the logarithmic term $\log(1+x)$ by its first-order Taylor series expansion, which gives x . Therefore, $\mathcal{P}_{2.1}$ is solved to tackle \mathcal{P}_2 .

Upon reformulating $\mathcal{P}_{2.1}$ as follows:

$$\mathcal{P}_{2.1}: \max_{0 \preceq \mathbf{m} \preceq \mathbf{1}} \sum_{k=1}^K \left(\frac{\mathbf{m}^T \Re \left(\Sigma_k^{\mathcal{P}_2} \right) \mathbf{m}}{\mathbf{m}^T \Re \left(\tilde{\Sigma}_k^{\mathcal{P}_2} \right) \mathbf{m} + \sigma^2} \right), \quad (29)$$

where we have $\mathbf{m} = \mathbf{M}^T \mathbf{1}_{N_t}$, the matrices $\Sigma_k^{\mathcal{P}_2}$ and $\tilde{\Sigma}_k^{\mathcal{P}_2}$ are defined as

$$\Sigma_k^{\mathcal{P}_2} = \text{diag}(\mathbf{V} \mathbf{f}_k) \mathbf{h}_{tot,k} \mathbf{h}_{tot,k}^H \text{diag}(\mathbf{V} \mathbf{f}_k)^H, \quad (30)$$

$$\tilde{\Sigma}_k^{\mathcal{P}_2} = \text{diag}(\mathbf{V} \mathbf{f}_{k'}) \mathbf{h}_{tot,k} \mathbf{h}_{tot,k}^H \text{diag}(\mathbf{V} \mathbf{f}_{k'})^H. \quad (31)$$

Algorithm 1: Alternating maximization algorithm

Input: Initialize digital beamformer matrix $\mathbf{F}^{(0)}$, holographic beamformer matrix $\mathbf{M}^{(0)}$ and RIS phase shift matrix $\Theta_{RIS}^{(0)}$. Set $t = 1$.

Output: Optimal \mathbf{F} , \mathbf{M} and Θ_{RIS}

- 1 Compute the digital beamformer matrix $\mathbf{F}^{(t)}$ using $\mathbf{M}^{(t-1)}$, $\Theta_{RIS}^{(t-1)}$ and (24).
 - 2 Compute the holographic beamformer matrix $\mathbf{M}^{(t)}$ using $\mathbf{F}^{(t)}$, $\Theta_{RIS}^{(t-1)}$ and (32).
 - 3 Compute the RIS phase shift matrix $\Theta_{RIS}^{(t)}$ using $\mathbf{F}^{(t)}$, $\mathbf{M}^{(t)}$ and the Riemannian conjugate gradient algorithm to solve (37).
 - 4 Set $t = t + 1$;
 - 5 **repeat steps 1 to 4**
 - 6 **until** The value of the objective function in (19) converges or maximum iteration reached.
-

Note that $\mathcal{P}_{2.1}$ is still nonconvex due to the fractional quadratic objective function. Hence, we simplify it by harnessing the first-order Taylor approximation as

$$\mathcal{P}_{2.2} : \max_{\mathbf{0} \preceq \mathbf{m} \preceq \mathbf{1}} \sum_{k=1}^K \left(\frac{2\mathbf{m}^{(0)T} \Re(\Sigma_k^{\mathcal{P}_2}) \mathbf{m} - \mathbf{m}^{(0)T} \Re(\Sigma_k^{\mathcal{P}_2}) \mathbf{m}^{(0)}}{\mathbf{m}^T \Re(\tilde{\Sigma}_k^{\mathcal{P}_2}) \mathbf{m} + \sigma^2} \right), \quad (32)$$

where $\mathcal{P}_{2.2}$ is a standard fractional maximization problem that can be solved using the popular Dinkelbach-based method [51]. The Algorithm 2 in Appendix summarizes the solving method for problem $\mathcal{P}_{2.2}$.

D. RIS Phase Shift Matrix Design (\mathcal{P}_3)

Next we focus on the RIS phase optimization subproblem. For ease of representation, we define the effective channels for the direct link and the RIS link. From (12) and (13) we have

$$\begin{aligned} y_k &= \mathbf{h}_{\text{tot},k}^H \mathbf{M}_v \mathbf{F} \mathbf{s} + n_k, \\ &= \underbrace{\mathbf{h}_{d,k}^H \mathbf{M}_v \mathbf{F} \mathbf{s}}_{\text{Direct link}} + \underbrace{\mathbf{h}_{R,k}^H \Theta_{RIS} \mathbf{G}_R \mathbf{M}_v \mathbf{F} \mathbf{s}}_{\text{RIS-aided link}} + n_k, \\ &= (\mathbf{h}_{d,k}^H + \mathbf{h}_{R,k}^H \Theta_{RIS} \mathbf{G}_R) \mathbf{M}_v \mathbf{F} \mathbf{s} + n_k, \\ &= (\mathbf{h}_{d,k}^H + \mathbf{h}_{R,k}^H \Theta_{RIS} \mathbf{G}_R) \mathbf{M}_v \sum_{k=1}^K \mathbf{f}_k s_k + n_k. \end{aligned} \quad (33)$$

To make expression (33) more tractable, we further define $\Theta_{RIS} = [e^{j\theta_1}, \dots, e^{j\theta_{N_{RIS}}}]^H$ and $\mathbf{H}_{R,k} = \text{diag}(\mathbf{h}_{R,k}^H) \mathbf{G}_R$. The received signal y_k is equivalently represented as

$$y_k = (\mathbf{h}_{d,k}^H + \Theta_{RIS}^H \mathbf{H}_{R,k}) \mathbf{M}_v \sum_{k=1}^K \mathbf{f}_k s_k + n_k. \quad (34)$$

For the sake of notational simplicity, let us define the effective channels for the direct link and the RIS link as follows:

$$\mathbf{a}_{k',k} = \mathbf{H}_{R,k} \mathbf{M}_v \mathbf{f}_{k'}, \quad (35)$$

$$b_{k',k} = \mathbf{h}_{d,k}^H \mathbf{M}_v \mathbf{f}_{k'}, \quad (36)$$

respectively. The phase optimization subproblem \mathcal{P}_3 can be expressed as a function of Θ_{RIS} as follows:

$$\mathcal{P}_3 : \max_{\{\Theta_{RIS}\}} f(\Theta_{RIS}) \quad \text{s.t. } |\Theta_{RIS}(i)|^2 = 1, \quad \forall i = 1, \dots, N_{RIS} \quad (37)$$

where we have:

$$\begin{aligned} f(\Theta_{RIS}) &= \sum_{k=1}^K R_k, \\ &= \sum_{k=1}^K \log_2 \left(1 + \frac{|\Theta_{RIS}^H \mathbf{a}_{k,k} + b_{k,k}|^2}{\sum_{k' \neq k} |\Theta_{RIS}^H \mathbf{a}_{k',k} + b_{k',k}|^2 + \sigma^2} \right). \end{aligned} \quad (38)$$

It can be observed that $f(\Theta_{RIS})$ is both continuous and differentiable. Additionally, the constraint set of Θ_{RIS} forms a complex circle manifold. Consequently, the stationary solution of \mathcal{P}_3 can be obtained via the Riemannian conjugate gradient algorithm [40]. The Riemannian conjugate gradient algorithm exhibits better robustness to initialization than the family of gradient-based methods in Euclidean spaces. Due to the constant modulus constraint in (37), the problem is known to be NP-hard. Other approaches, such as the semi-definite relaxation with randomization, and the majorization-minimization framework, could also be used, but they incur relatively high computational costs due to the non-convex constant modulus constraint. The Riemannian conjugate gradient algorithm naturally incorporates the physical constraints of RIS systems, such as the constant modulus constraint, making it particularly effective in handling the complex non-convex optimization problems associated with RIS phase shifts on a manifold. Conceptually, the Riemannian conjugate gradient algorithm involves three key steps in each iteration:

1) *Compute the Riemannian Gradient:* For a smooth function f defined on a Riemannian manifold \mathcal{M} , the Riemannian gradient ($\text{grad}f$) is the orthogonal projection of the Euclidean gradient ∇f onto the complex circle formulated as:

$$\text{grad}f = \nabla f - \text{Re} \{ \nabla f \circ \Theta_{RIS}^* \} \circ \Theta_{RIS}, \quad (39)$$

where the Euclidean gradient is

$$\nabla f = \sum_{k=1}^K 2\mathbf{A}_k, \quad (40)$$

in conjunction with

$$\begin{aligned} \mathbf{A}_k &= \frac{\sum_{k'} \mathbf{a}_{k',k} \mathbf{a}_{k',k}^H \Theta_{RIS} + \sum_{k'} \mathbf{a}_{k',k} b_{k',k}^*}{\sum_{k'} |\Theta_{RIS}^H \mathbf{a}_{k',k} + b_{k',k}|^2 + \sigma^2} \\ &\quad - \frac{\sum_{k' \neq k} \mathbf{a}_{k',k} \mathbf{a}_{k',k}^H \Theta_{RIS} + \sum_{k' \neq k} \mathbf{a}_{k',k} b_{k',k}^*}{\sum_{k' \neq k} |\Theta_{RIS}^H \mathbf{a}_{k',k} + b_{k',k}|^2 + \sigma^2}. \end{aligned} \quad (41)$$

2) *Search Direction:* In general, the search direction is given by the opposite of the Riemannian gradient. The tangent vector conjugate of $\text{grad}f$ gives the search direction:

$$\boldsymbol{\eta} = -\text{grad}f + \beta_1 \mathcal{T}(\bar{\boldsymbol{\eta}}), \quad (42)$$

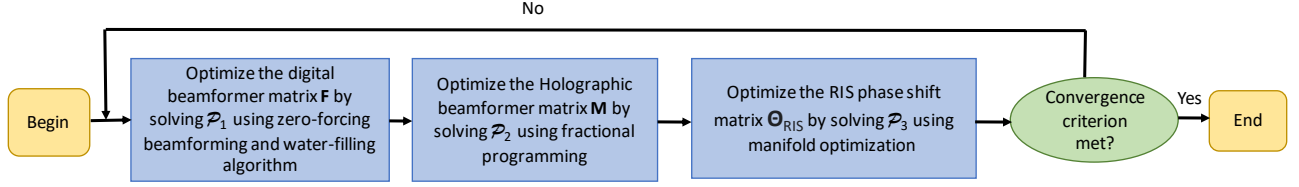


Fig. 2: Flow chart of the proposed AM algorithm for sum-rate.

where $\mathcal{T}(\cdot)$ is the vector transport function defined as

$$\mathcal{T}(\eta) = \bar{\eta} - \text{Re}\{\eta \circ \theta_{RIS}^*\} \circ \theta_{RIS}, \quad (43)$$

while β_1 is the conjugate gradient update parameter, and $\bar{\eta}$ is the previous search direction.

3) *Retraction*: The retraction step updates the current point on the manifold using the search direction to ensure that the next iteration remains on the manifold. By projecting the tangent vector back to the complex circle manifold we get

$$\theta_{RIS}(n) \leftarrow \frac{(\theta_{RIS} + \beta_2 \eta)_n}{|(\theta_{RIS} + \beta_2 \eta)_n|}, \quad (44)$$

where $\theta_{RIS}(n)$ represents the n -th component of the vector θ_{RIS} and β_2 is the Armijo step size, which determines the size of the step taken along the search direction in each iteration.

To gain a clear understanding of the variable updating process in each step, please refer to the detailed procedure formulated by Algorithm in 1.

E. Computational Complexity

In this section we first calculate the complexity of the algorithms for three subproblems separately and then compute the overall computational complexity of the alternating maximization algorithm in 1.

- For the update of the digital beamforming matrix \mathbf{F} , we use the zero-forcing algorithm to mitigate interference by applying a pseudo-inverse of the channel matrix to the received signal. The complexity of this step is $\mathcal{O}(K^2 N_{RF})$. The normalization factor ϵ is obtained by solving the equation $\sum_{k=1}^K \max\{\frac{1}{\epsilon} - \mu_k \sigma^2, 0\} = P_T$, which has a complexity of $\mathcal{O}(K^2)$. Following that, the optimal received power p_k^* is obtained by (26) with a complexity of $\mathcal{O}(K)$. Therefore, the total complexity of the digital beamforming is $\mathcal{O}(K^2 N_{RF})$.
- At each inner iteration of the Dinkelbach-based method, the problem is solved by CVX using the interior-point method, which generally has a complexity of $\mathcal{O}(N_t^3)$ for the update of the holographic beamformer matrix \mathbf{M} . Given a total of l_M inner iterations in Algorithm 2, the complexity is $\mathcal{O}(l_M N_t^3)$.
- To update the RIS phase shift matrix Θ_{RIS} , we use the Riemannian conjugate gradient algorithm. The complexity of the Riemannian conjugate gradient algorithm is dominated by the computation of the Euclidean gradient, which is $\mathcal{O}(K^2 N_{RIS}^2)$. The retraction step also requires iteratively searching for β_2 with a complexity

of $\mathcal{O}(K^2 N_{RIS})$, which can be ignored when N_{RIS} is large.

Therefore the total complexity for each outer iteration of the proposed AM algorithm is $\mathcal{O}(K^2 N_{RF} + l_M N_t^3 + K^2 N_{RIS}^2)$.

F. Convergence

In the AM Algorithm 1 convinced for digital beamforming, the sum-rate (R_{sum}) in (18) becomes non-decreasing after optimizing the digital beamformer matrix \mathbf{F} , given the holographic beamformer $\mathbf{M}^{(t-1)}$ and RIS phase shift matrix $\Theta_{RIS}^{(t-1)}$ in the t -th iteration, i.e.,

$$R_{sum}(\mathbf{F}^{(t)}, \mathbf{M}^{(t-1)}, \Theta_{RIS}^{(t-1)}) \geq R_{sum}(\mathbf{F}^{(t-1)}, \mathbf{M}^{(t-1)}, \Theta_{RIS}^{(t-1)}). \quad (45)$$

Secondly, given the digital beamformer matrix $\mathbf{F}^{(t)}$ and the RIS phase shift matrix $\Theta_{RIS}^{(t-1)}$, the holographic beamformer matrix $\mathbf{M}^{(t-1)}$ is optimized using an algorithm proposed in 2, so that we obtain

$$R_{sum}(\mathbf{F}^{(t)}, \mathbf{M}^{(t)}, \Theta_{RIS}^{(t-1)}) \geq R_{sum}(\mathbf{F}^{(t)}, \mathbf{M}^{(t-1)}, \Theta_{RIS}^{(t-1)}). \quad (46)$$

After updating the two variables, given the digital beamformer matrix $\mathbf{F}^{(t)}$ and the holographic beamformer matrix $\mathbf{M}^{(t)}$, the RIS phase shift matrix $\Theta_{RIS}^{(t-1)}$ is optimized using manifold optimization. Consequently, we obtain

$$R_{sum}(\mathbf{F}^{(t)}, \mathbf{M}^{(t)}, \Theta_{RIS}^{(t)}) \geq R_{sum}(\mathbf{F}^{(t)}, \mathbf{M}^{(t)}, \Theta_{RIS}^{(t-1)}). \quad (47)$$

This means that in each update step of the proposed algorithm, the objective function value (i.e., sum-rate) does not decrease. Additionally, the sequence of objective function values obtained during the iteration steps is both monotonic and bounded, ensuring that the overall algorithm will converge.

G. Power Consumption and Hardware Cost

In this section, we compare the power consumption and hardware cost of phased array and RHS systems. Let us consider the hardware cost of a phased array module as ξ_{ph} and the hardware cost of an RHS module as ξ_{rhs} . We define the cost ratio C_r as the ratio of the phased array's cost to the RHS cost, i.e., $C_r = \frac{\xi_{ph}}{\xi_{rhs}}$. For a phased array system with N_t antennas, the hardware cost is $N_t C_r \xi_{rhs}$. Similarly, for an RHS system having N_t elements, the total hardware cost is $N_t \xi_{rhs}$. In the RHS prototype [52], it is shown that in array grids, RHSs typically have about 2.5 times as many elements as a phased array system having the same antenna directivity. Additionally, the radiation power to total power

consumption for phased array and RHS systems is 4% and 25%, respectively. In this case, the total hardware cost of an RHS system is $2.5N_t\xi_{rhs}$ and for the phased array system, it is $N_tC_r\xi_{rhs}$. Given that the typical value of C_r is 10 [52], the hardware cost of the phased array system is higher than that of the RHS system. This demonstrates that RHS provides a powerful solution to reduce hardware costs with lower power consumption, while guaranteeing better directivity in practice.

IV. SIMULATION RESULTS

In this section, we present simulation results for characterizing the performance of the proposed approach. We focus exclusively on the far-field region, as both the RIS and UEs are positioned beyond the Rayleigh distance ($D_R = 2D^2/\lambda$) from the BS, where D denotes the array aperture. The AM algorithm put forward in this study leverages perfect channel state information (CSI) to achieve the optimal sum-rate for the system.

TABLE II: Simulation Parameters

Parameters	Values
Number of RHS elements (N_t)	16 to 64
Number of RIS elements (N_{RIS})	20 to 100
Number of RF chains (N_{RF})	8
Number of UEs (K)	2 to 4
Number of antennas at each UE	1
Number of multipaths (L_d, L_{br}, L_{ru})	10
Operating frequency (f_c) in GHz	28
Distance between the RIS elements ($d = \lambda/2$) in cm	0.53
Distance between the RHS elements ($d = \lambda/4$) in cm	0.265
Transmit power of the BS (P_T) in W	3 to 30
Noise power (dBm)	-90
Path loss for LOS link (dB)	$61.4 + 20 \log(d_i) + 5.8$
Path loss for NLOS link (dB)	$72 + 29.2 \log(d_i) + 8.7$

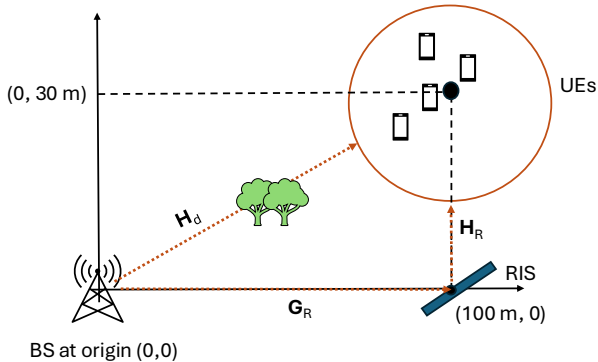


Fig. 3: Overview of the simulated RHS-RIS system having K UEs with one receive antenna, a BS with N_t RHS elements and an RIS with N_{RIS} elements.

The simulations rely on a configuration, where random initial values are assigned to \mathbf{F} , \mathbf{M} , and Θ_{RIS} . The iterative

process of updating one variable, while holding the others constant is applied to all three variables. This iterative procedure continues until a specified stopping criterion is satisfied, as defined in Algorithm 1. The solutions to the three subproblems optimizing \mathbf{F} , \mathbf{M} , and Θ_{RIS} are either near-optimal or locally optimal, as analyzed in the previous subsections. Therefore, the term ‘optimal’ describes the best solution obtained within the constraints of a specific algorithm, but it does not necessarily represent the global optimum of the overall problem. The parameters used for the simulations are given in Table II. The simulation results are averaged over 100 independent channel realizations. The wireless channels are generated using the mmWave channel model (3) discussed in Section II. The flow chart of the joint sum-rate optimization algorithm is summarized in Fig. 2. We compare the performance of the proposed method to a range of benchmark schemes: (a) an RHS system without an RIS, and (b) an RHS system with a randomly configured RIS. In the latter case, we consider a random selection of the passive RIS phase shift matrix Θ_{RIS} . For a fair comparison, we employ the same objective function and constraints across all benchmark schemes, using the sum-rate as the performance metric.³

The BS is equipped with $N_t = 64$ elements located at (0m, 0m), and 4 single-antenna UEs ($K = 4$) uniformly and randomly distributed in a circle centered at (100m, 30m) with radius 10 m. We assume that the RIS is deployed at (100m, 0m), and the UEs location is fixed once randomly generated as shown in Fig. 3. The N_{RF} RF chains are connected to the N_t RHS elements through N_{RF} feeds that convert the carrier frequency current into an electromagnetic wave. This wave propagates through the waveguide of the RHS and radiates the energy into the free space from the N_t RHS elements, as shown in Fig. 1.

For the mmWave model, the channel gains α_{l_*} are generated independently, following the distribution $\alpha_{l_*} \sim \mathcal{CN}(0, 10^{-0.1PL(d_i)})$. The quantity $PL(d_i)$ represents the path loss dependent on the distance d_i associated with the corresponding link. The modified path loss model described in [4] is considered, and the path loss in dB is given by the following equation

$$PL(d_i) = a + 10b \log_{10}(d_i) + \kappa, \quad (48)$$

where $\kappa \in \mathcal{CN}(0, \sigma_\kappa^2)$. The values of a, b and σ_κ^2 are set to $a = 61.4, b = 2$ and $\sigma_\kappa^2 = 5.8$ dB for the line-of-sight paths. For the non-line-of-sight (NLOS) paths, the values are set to $a = 72, b = 2.92$ and $\sigma_\kappa^2 = 8.7$ dB. To evaluate the effectiveness of the RIS more accurately, we assume that each path of \mathbf{H}_d is a NLOS path that faces partial blockage from obstacles and experiences an additional penetration loss of 40 dB. The carrier frequency (f_c) is set to 28 GHz, the bandwidth (B) is set to 250 MHz and thus the noise power is $-174 + 10 \log_{10}B = -90$ dBm. For simplicity, we consider each UE to experience the same number of paths from both the BS and the RIS. Moreover, we set the number of paths to $L_i = 10, i \in \{d, ru, bu\}$. The antenna spacing at the RHS and RIS is set to $d = \lambda/4$ and $\lambda/2$, respectively.

³In the simulation, the UE locations are (98.3m, 27.8m), (99.8m, 30.1m), (100.2m, 30.7m) and (99m, 32.9m)

The RIS is applied to provide a high-quality link between the BS and UEs, where we assume that the LOS component is included in the channel between the BS and RIS, and in the channel between the RIS and each UE. Benefited from the directional reflections of the RIS, the BS-RIS-UE link is usually stronger than other multipaths as well as the degraded direct link between the BS and the UE. Five iterations of the proposed algorithm have been considered in this analysis. In each iteration, the three sub problems are solved alternatively.

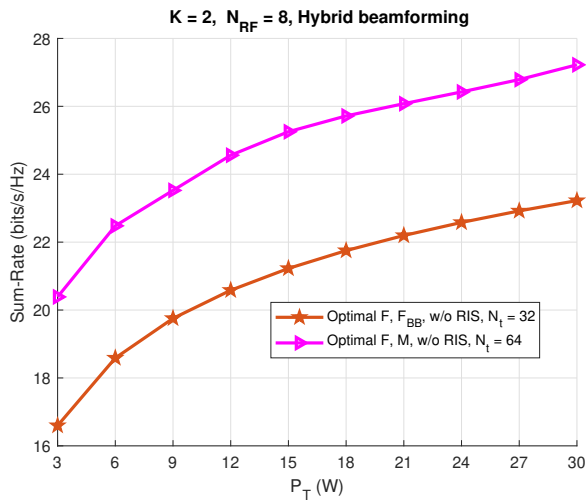


Fig. 4: The sum-rate for hybrid beamforming using active phased arrays and holographic beamforming is compared across different values of P_T for the case where $K = 4$.

In Fig. 4, the sum-rate comparison for hybrid beamforming using active phased arrays and holographic beamforming without an RIS is presented across different P_T values for $K = 2$. The analog beamforming matrix using active phased arrays is represented by \mathbf{F}_{BB} with the distance between elements set to $\lambda/2$. In contrast, for holographic beamforming, the distance between RHS elements is $\lambda/4$. This allows for twice the number of smaller RHS elements to be accommodated within the same space. It is evident that the sum-rate gain is consistently higher when using holographic beamforming compared to analog beamforming with active phased arrays.

In Figs. 5a, 5b, and 5c, the sum-rate is illustrated for $K = 2, 3$ and 4 and for different P_T values. It can be observed that when there is no RIS in the system, the performance gain in sum-rate is always less than that of the system relying on an RIS. If the phase shift matrix Θ_{RIS} is not optimized, the performance gain achieved by deploying an RIS is insignificant, as expected. For example, observe in Fig. 5c that hybrid beamforming and the phase optimization scheme applied by the system achieve about 13 bps/Hz improvement in sum-rate at $P_T = 15$ W. It is observed that the proposed algorithm relying on an optimized phase shift matrix Θ_{RIS} exhibits the highest sum-rate for all the values of P_T across all methods. Clearly, for higher values of P_T at the BS we can have an increased sum-rate, while keeping the remaining system parameters constant.

In Fig. 6 the sum-rate is illustrated for $K = 2, 3$ and 4 and for a P_T value of 15 W. Again, it can be observed that when

there is no RIS in the system and when using a random phase shift matrix, the sum-rate gain is always less than that of the system with an optimized RIS. For example, in Fig. 6, the system achieves about 11.5 bps/Hz improvement in sum-rate at $K = 3$ upon using phase optimization. It is also observed that the proposed algorithm having an optimized phase shift matrix Θ_{RIS} exhibits the highest sum-rate for all the values of K for all methods. Clearly, for higher values of K at the BS we have an increased sum-rate, while keeping the remaining system parameters constant.

In Fig. 7, a comparison of the sum-rate is illustrated for N_{RIS} ranging from 20 to 100 with a P_T value of 15 W. Once again, it is evident that the sum-rate gain is consistently lower, when using a random phase shift matrix compared to a system with an optimized phase shift matrix Θ_{RIS} for all values of N_{RIS} . Clearly, for higher values of N_{RIS} we have an increased sum-rate, while keeping the remaining system parameters constant.

In Fig. 8, a comparison of the sum-rate is illustrated for RHS elements ranging from 16 to 64 with a P_T value of 15 W. With an optimized phase shift matrix, increasing the number of RHS elements from 16 to 64 results in a sum-rate improvement of 13 bps/Hz. Once again, it can be observed that in the absence of an RIS and when using a random phase shift matrix, the sum-rate gain is consistently lower than that achieved by the system having an optimized phase shift matrix Θ_{RIS} for all values of N_t . Clearly, for higher values of N_t , we have an increased sum-rate, while keeping the remaining system parameters constant.

Fig. 9 presents a comparison of the sum-rate for both perfect and imperfect CSI, evaluating the robustness of the proposed sum-rate maximization algorithm against channel estimation errors [17], [21]. In the imperfect CSI case, we assume that the channel matrix from the RHS to the k -th UE \mathbf{H}_k , lies within a ball of radius $0.1\|\mathbf{H}_k\|$ around the estimated channel matrix, $\hat{\mathbf{H}}_k$. This is expressed as $\mathbf{H}_k = \{\hat{\mathbf{H}}_k + \delta_k \mid \|\delta_k\| \leq 0.1\|\mathbf{H}_k\|\}$, where δ_k represents the channel estimation error, with its norm assumed to be bounded by $0.1\|\mathbf{H}_k\|$. A slight drop in the sum-rate can be observed, indicating the inherent robustness of the proposed algorithm against channel estimation errors.

In Fig. 10, the sum-rate in the presence of mutual coupling is illustrated for $K = 4$ across different P_T values. It can be observed that when the distance between the RHS elements is $\lambda/4$ and the system operates at mmWave frequencies, the high mutual coupling leads to a significant loss in sum-rate performance. However, the proposed algorithm, which relies on an optimized phase shift matrix Θ_{RIS} consistently achieves the highest sum-rate for all P_T values across all methods, even in the presence of mutual coupling. This demonstrates that our proposed method performs well in both scenarios, regardless whether mutual coupling is present or absent.

V. SUMMARY AND CONCLUSION

We proposed a novel AM algorithm designed for maximizing the sum-rate of a mmWave multi-UE system. The proposed manifold optimization-based AM algorithm leveraged all the new wireless technologies like RHS and RIS in the face of a

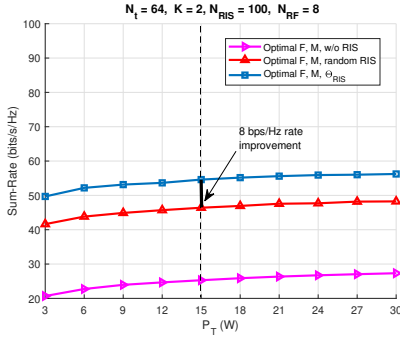
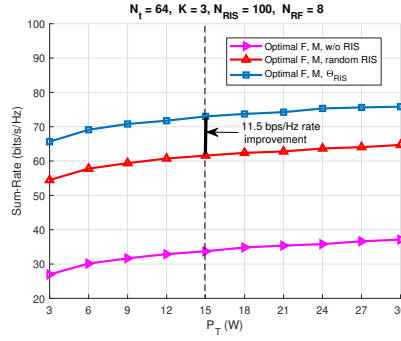
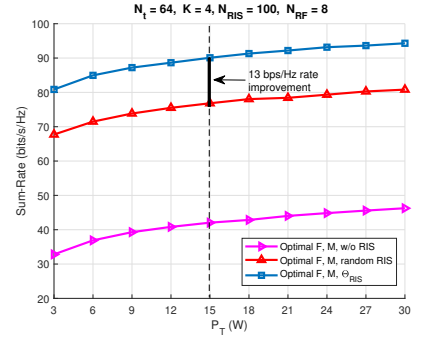
(a) $K = 2$ (b) $K = 3$ (c) $K = 4$

Fig. 5: The sum-rate is compared across different values of P_T for the case where $K = 2, 3$ and 4 , considering a given set of parameters including N_t, N_{RF} , and N_{RIS}

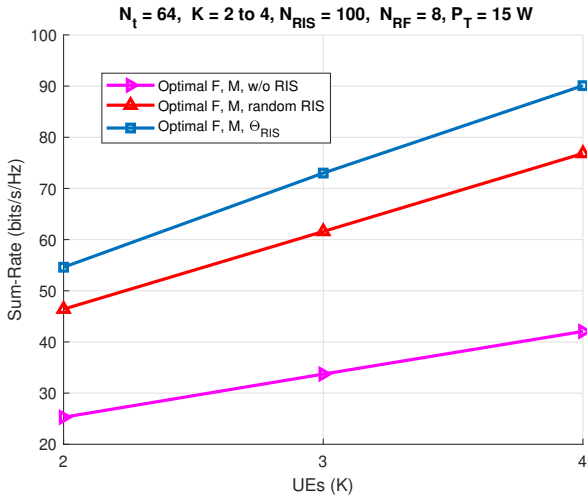


Fig. 6: The sum-rate is compared across different UEs for a given set of parameters including N_t, N_{RF}, N_{RIS} and P_T .

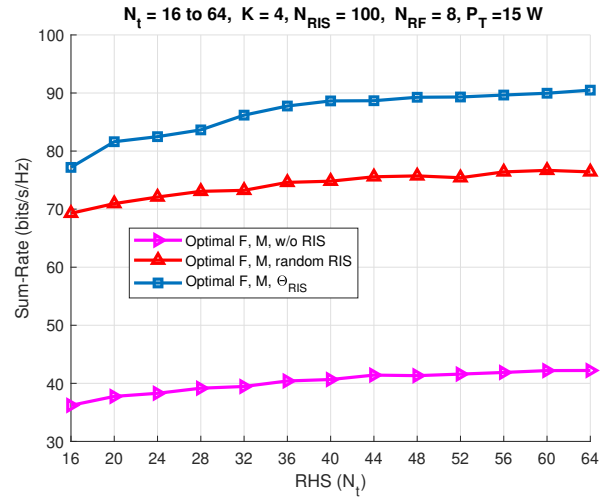


Fig. 8: The sum-rate is compared across different N_t RHS elements, for a given set of parameters including N_{RF}, K and P_T .

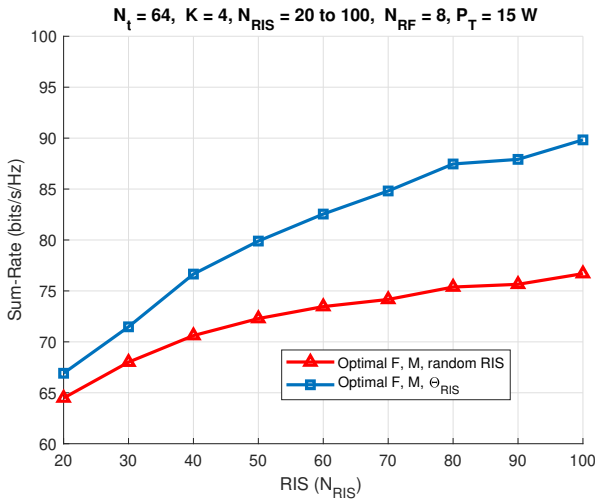


Fig. 7: The sum-rate is compared across different N_{RIS} for a given set of parameters including N_t, N_{RF}, K and P_T .

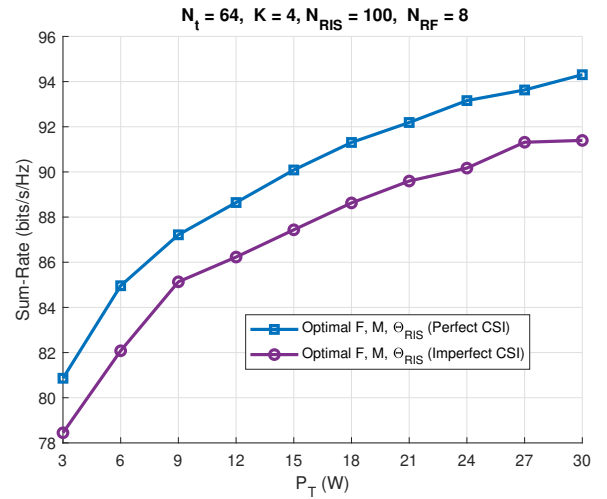


Fig. 9: The sum-rate for both perfect and imperfect CSI is compared across different values of P_T for the case where $K = 4$.

mmWave channel. The numerical results revealed a significant enhancement in the sum-rate when employing our proposed algorithm. The sum-rate improvement attained ranges from

8 bps/Hz to 13 bps/Hz for K values ranging from 2 to 4 and for various P_T values, which is significant. This confirms the effectiveness of our algorithm over existing methods in

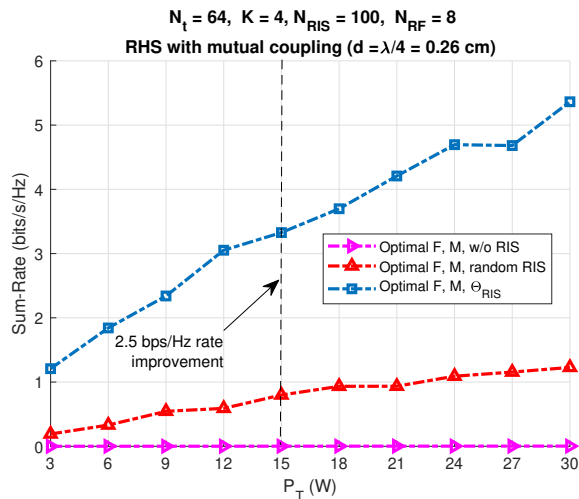


Fig. 10: The sum-rate in the presence of mutual coupling, generated using (16) for a distance of $\lambda/4 = 0.26$ cm between the RHS elements, is compared across different values of P_T for the case where $K = 4$.

mmWave multi-UE systems.

VI. ACKNOWLEDGEMENT

Pavan Kumar Gadamsetty and K.V.S. Hari would like to acknowledge the support of the British Telecom India Research Centre (BTIRC), Indian Institute of Science, Bangalore.

L. Hanzo would like to acknowledge the financial support of the Engineering and Physical Sciences Research Council (EPSRC) projects under grant EP/Y037243/1, EP/W016605/1, EP/X01228X/1, EP/Y026721/1, EP/W032635/1 and EP/X04047X/1 as well as of the European Research Council's Advanced Fellow Grant QuantCom (Grant No. 789028).

APPENDIX

In the Dinkelbach-based method, $\mathbf{m}^{(0)}$ represents the randomly initialized value of \mathbf{m} , Σ^{P_2} is defined as the summation of $\Sigma_k^{P_2}$ for k from 1 to K , and $\tilde{\Sigma}^{P_2}$ is defined as the summation of $\tilde{\Sigma}_k^{P_2}$ for k from 1 to K . The optimal value of \mathbf{m} obtained after solving (32) using Algorithm 2 is denoted by \mathbf{m}^* . Dinkelbach method can be convergent to the global optimal solution [53].

REFERENCES

- [1] C.-X. Wang, X. You, X. Gao, X. Zhu, Z. Li, C. Zhang, H. Wang, Y. Huang, Y. Chen, H. Haas, *et al.*, "On the road to 6G: Visions, requirements, key technologies, and testbeds," *IEEE Commun. Surv. Tutor.*, vol. 25, no. 2, pp. 905–974, 2023.
- [2] Z. Ma, M. Xiao, Y. Xiao, Z. Pang, H. V. Poor, and B. Vucetic, "High-reliability and low-latency wireless communication for Internet of Things: Challenges, fundamentals, and enabling technologies," *IEEE Internet Things J.*, vol. 6, no. 5, pp. 7946–7970, 2019.
- [3] T. S. Rappaport, J. N. Murdock, and F. Gutierrez, "State of the art in 60-GHz integrated circuits and systems for wireless communications," *Proc. of the IEEE*, vol. 99, no. 8, pp. 1390–1436, 2011.
- [4] I. A. Hemadeh, K. Satyanarayana, M. El-Hajjar, and L. Hanzo, "Millimeter-wave communications: Physical channel models, design considerations, antenna constructions, and link-budget," *IEEE Commun. Surv. Tutor.*, vol. 20, no. 2, pp. 870–913, 2017.

Algorithm 2: Dinkelbach-based solver for (32)

Input: Σ^{P_2} , $\tilde{\Sigma}^{P_2}$, ζ , $\mathbf{m}^{(0)}$

Output: \mathbf{m}^*

- 1 Set $t = 0$, $\lambda_t = 0$ and $\mathbf{m}_t = \mathbf{m}^{(0)}$
- 2 **repeat**
- 3 Find the optimal solution \mathbf{m}_t by solving problem (32) using CVX.
- 4 Let $F_{\lambda_t} = 2\mathbf{m}^{(0)T} \Re(\Sigma^{P_2}) \mathbf{m}_t - \lambda_t \mathbf{m}_t^T \Re(\tilde{\Sigma}^{P_2}) \mathbf{m}_t$;
- 5 Set $t = t + 1$;
- 6 Update $\lambda_t = \frac{2\mathbf{m}^{(0)T} \Re(\Sigma^{P_2}) \mathbf{m}_t - \mathbf{m}^{(0)T} \Re(\Sigma^{P_2}) \mathbf{m}^{(0)}}{\mathbf{m}_t^T \Re(\Sigma^{P_2}) \mathbf{m}_t + \sigma^2}$;
- 7 **until** $F_{\lambda_t} \leq \zeta$ or maximum iterations reached
- 8 **return** $\mathbf{m}^* = \mathbf{m}_t$

- [5] M. Ragheb, A. Kuhestani, M. Kazemi, H. Ahmadi, and L. Hanzo, "RIS-aided secure millimeter-wave communication under RF-chain impairments," *IEEE Trans. Veh. Technol.*, vol. 73, no. 1, pp. 952–963, 2024.
- [6] Y. Chen, X. Guo, Z. Wang, and C. Yuen, "Unifying far-field and near-field wireless communications in 6G MIMO," *IEEE Wireless Commun. Lett.*, 2024.
- [7] X. Mu, J. Xu, Y. Liu, and L. Hanzo, "Reconfigurable intelligent surface-aided near-field communications for 6G: Opportunities and challenges," *IEEE Veh. Technol. Mag.*, pp. 2–11, 2024.
- [8] C. Huang, A. Zappone, G. C. Alexandropoulos, M. Debbah, and C. Yuen, "Reconfigurable intelligent surfaces for energy efficiency in wireless communication," *IEEE Trans. Wireless Commun.*, vol. 18, no. 8, pp. 4157–4170, 2019.
- [9] H. Tuan, A. Nasir, E. Dutkiewicz, H. V. Poor, and L. Hanzo, "RIS-aided Multiple-Input Multiple-Output broadcast channel capacity," *IEEE Trans. Commun.*, vol. 72, no. 1, pp. 117–132, 2024.
- [10] F. Liu, D.-H. Kwon, and S. Tretyakov, "Reflectarrays and metasurface reflectors as diffraction gratings: A tutorial," *IEEE Antenn. Propag. Mag.*, vol. 65, no. 3, pp. 21–32, 2023.
- [11] Q. Wu and R. Zhang, "Towards smart and reconfigurable environment: Intelligent reflecting surface aided wireless network," *IEEE Commun. Mag.*, vol. 58, no. 1, pp. 106–112, 2020.
- [12] H. Zhu, S. Cheung, K. L. Chung, and T. I. Yuk, "Linear-to-circular polarization conversion using metasurface," *IEEE Trans. Antennas Propag.*, vol. 61, no. 9, pp. 4615–4623, 2013.
- [13] K. V. Mishra, J. A. Hodge, and A. I. Zaghoul, "Reconfigurable metasurfaces for radar and communications systems," in *Proc. URSI Asia-Pacific Radio Sci. Conf. (AP-RASC)*, pp. 1–4, 2019.
- [14] S. Zhang, C. Guo, T. Wang, and W. Zhang, "On-off analog beamforming for massive MIMO," *IEEE Trans. Veh. Technol.*, vol. 67, no. 5, pp. 4113–4123, 2018.
- [15] S. Wan, H. Zhu, K. Kang, and H. Qian, "On the performance of fully-connected and sub-connected hybrid beamforming system," *IEEE Trans. Veh. Technol.*, vol. 70, no. 10, pp. 11078–11082, 2021.
- [16] X. Yu, J.-C. Shen, J. Zhang, and K. B. Letaief, "Alternating minimization algorithms for hybrid precoding in millimeter wave MIMO systems," *IEEE J. Sel. Top. Signal Process.*, vol. 10, no. 3, pp. 485–500, 2016.
- [17] H. Guo, Y.-C. Liang, J. Chen, and E. G. Larsson, "Weighted sum-rate maximization for reconfigurable intelligent surface aided wireless networks," *IEEE Trans. Wireless Commun.*, vol. 19, no. 5, pp. 3064–3076, 2020.
- [18] H. Niu, Z. Chu, F. Zhou, Z. Zhu, M. Zhang, and K.-K. Wong, "Weighted sum secrecy rate maximization using intelligent reflecting surface," *IEEE Trans. Commun.*, vol. 69, no. 9, pp. 6170–6184, 2021.
- [19] Q. Li, M. El-Hajjar, I. Hemadeh, A. Shojafard, A. A. Mourad, B. Clerckx, and L. Hanzo, "Reconfigurable intelligent surfaces relying on non-diagonal phase shift matrices," *IEEE Trans. Veh. Technol.*, vol. 71, no. 6, pp. 6367–6383, 2022.
- [20] J. Singh, S. Srivastava, A. K. Jagannatham, and L. Hanzo, "Joint transceiver and reconfigurable intelligent surface design for multiuser mmWave MIMO systems relying on non-diagonal phase shift matrices," *IEEE Open J. Commun. Soc.*, 2023.

- [21] R. Deng, B. Di, H. Zhang, Y. Tan, and L. Song, "Reconfigurable holographic surface-enabled multi-user wireless communications: Amplitude-controlled holographic beamforming," *IEEE Trans. Wireless Commun.*, vol. 21, no. 8, pp. 6003–6017, 2022.
- [22] W. Ren, J. Deng, and X. Cheng, "MMSE hybrid beamforming for multi-user millimeter wave MIMO systems," *IEEE Commun. Lett.*, 2023.
- [23] Y. Hu, H. Qian, K. Kang, X. Luo, and H. Zhu, "Joint precoding design for sub-connected hybrid beamforming system," *IEEE Trans. Wireless Commun.*, 2023.
- [24] Y. Liu, Y. Cai, A. Liu, M. Zhao, and L. Hanzo, "Latency minimization for mmWave D2D mobile edge computing systems: Joint task allocation and hybrid beamforming design," *IEEE Trans. Veh. Technol.*, vol. 71, no. 11, pp. 12206–12221, 2022.
- [25] C. Qi, Q. Liu, X. Yu, and G. Y. Li, "Hybrid precoding for mixture use of phase shifters and switches in mmWave massive MIMO," *IEEE Trans. Commun.*, vol. 70, no. 6, pp. 4121–4133, 2022.
- [26] L. You, X. Qiang, K.-X. Li, C. G. Tsinos, W. Wang, X. Gao, and B. Ottersten, "Hybrid analog/digital precoding for downlink massive MIMO LEO satellite communications," *IEEE Trans. Wireless Commun.*, vol. 21, no. 8, pp. 5962–5976, 2022.
- [27] C. Feng, W. Shen, J. An, and L. Hanzo, "Joint hybrid and passive RIS-assisted beamforming for mmWave MIMO systems relying on dynamically configured subarrays," *IEEE Internet Things J.*, vol. 9, no. 15, pp. 13913–13926, 2022.
- [28] Y. Pan, K. Wang, C. Pan, H. Zhu, and J. Wang, "Sum-rate maximization for intelligent reflecting surface assisted terahertz communications," *IEEE Trans. Veh. Technol.*, vol. 71, no. 3, pp. 3320–3325, 2022.
- [29] J. S. Herd and M. D. Conway, "The evolution to modern phased array architectures," *Proc. of the IEEE*, vol. 104, no. 3, pp. 519–529, 2015.
- [30] J. An, C. Yuen, C. Huang, M. Debbah, H. V. Poor, and L. Hanzo, "A tutorial on holographic MIMO communications—Part II: Performance analysis and holographic beamforming," *IEEE Commun. Lett.*, 2023.
- [31] R. Deng, B. Di, H. Zhang, H. V. Poor, and L. Song, "Holographic MIMO for LEO satellite communications aided by reconfigurable holographic surfaces," *IEEE J. Sel. Areas Commun.*, vol. 40, no. 10, pp. 3071–3085, 2022.
- [32] H. Zhang, H. Zhang, B. Di, M. Di Renzo, Z. Han, H. V. Poor, and L. Song, "Holographic integrated sensing and communication," *IEEE J. Sel. Areas Commun.*, vol. 40, no. 7, pp. 2114–2130, 2022.
- [33] T. Slesman, M. F. Imani, W. Xu, J. Hunt, T. Driscoll, M. S. Reynolds, and D. R. Smith, "Waveguide-fed tunable metamaterial element for dynamic apertures," *IEEE Antennas Wirel. Propag. Lett.*, vol. 15, pp. 606–609, 2016.
- [34] R. Deng, B. Di, H. Zhang, D. Niyato, Z. Han, H. V. Poor, and L. Song, "Reconfigurable holographic surfaces for future wireless communications," *IEEE Wireless Commun.*, vol. 28, no. 6, pp. 126–131, 2021.
- [35] Z. Wan, Z. Gao, F. Gao, M. Di Renzo, and M.-S. Alouini, "Terahertz massive MIMO with holographic reconfigurable intelligent surfaces," *IEEE Trans. Commun.*, vol. 69, no. 7, pp. 4732–4750, 2021.
- [36] T. Wei, L. Wu, K. V. Mishra, and M. B. Shankar, "RIS-aided wideband DFRC with reconfigurable holographic surface," in *Proc. ICASSP*, pp. 1–5, IEEE, 2023.
- [37] M.-y. Gong and B. Lyu, "Alternating maximization and the EM algorithm in maximum-likelihood direction finding," *IEEE Trans. Veh. Technol.*, vol. 70, no. 10, pp. 9634–9645, 2021.
- [38] A. Wiesel, Y. C. Eldar, and S. Shamai, "Zero-forcing precoding and generalized inverses," *IEEE Trans. Signal Process.*, vol. 56, no. 9, pp. 4409–4418, 2008.
- [39] K. Shen and W. Yu, "Fractional programming for communication systems—part I: Power control and beamforming," *IEEE Trans. Signal Process.*, vol. 66, no. 10, pp. 2616–2630, 2018.
- [40] N. Boumal, B. Mishra, P.-A. Absil, and R. Sepulchre, "Manopt, a MATLAB toolbox for optimization on manifolds," *J. Mach. Learn. Res.*, vol. 15, no. 1, pp. 1455–1459, 2014.
- [41] T. Gong, P. Gavrilidis, R. Ji, C. Huang, G. C. Alexandropoulos, L. Wei, Z. Zhang, M. Debbah, H. V. Poor, and C. Yuen, "Holographic MIMO communications: Theoretical foundations, enabling technologies, and future directions," *IEEE Commun. Surv. Tutor.*, 2023.
- [42] Q. Li, M. El-Hajjar, Y. Sun, I. Hemadeh, A. Shojaeifard, and L. Hanzo, "Energy-Efficient reconfigurable holographic surfaces operating in the presence of realistic hardware impairments," *IEEE Trans. Commun.*, 2024.
- [43] P. Wang, J. Fang, L. Dai, and H. Li, "Joint transceiver and large intelligent surface design for massive MIMO mmWave systems," *IEEE Trans. Wireless Commun.*, vol. 20, no. 2, pp. 1052–1064, 2020.
- [44] T. Wei, L. Wu, K. V. Mishra, and B. Shankar, "RIS-aided wideband holographic DFRC," *IEEE Trans. Aerosp. Electron. Syst.*, 2024.
- [45] P. Zheng, X. Ma, and T. Y. Al-Naffouri, "On the impact of mutual coupling on RIS-assisted channel estimation," *IEEE Wireless Commun. Lett.*, 2024.
- [46] Y. Liu, M. Zhang, T. Wang, A. Zhang, and M. Debbah, "Densifying MIMO: Channel modeling, physical constraints, and performance evaluation for holographic communications," *IEEE J. Sel. Areas Commun.*, 2024.
- [47] A. Pizzo, L. Sanguinetti, and T. L. Marzetta, "Fourier plane-wave series expansion for holographic MIMO communications," *IEEE Trans. Wireless Commun.*, vol. 21, no. 9, pp. 6890–6905, 2022.
- [48] P. Wang, M. N. Khormuji, and B. M. Popovic, "Beamforming performances of holographic surfaces," *IEEE Trans. Wireless Commun.*, 2023.
- [49] D. Tse and P. Viswanath, *Fundamentals of wireless communication*. Cambridge university press, 2005.
- [50] F. Sohrabi and W. Yu, "Hybrid digital and analog beamforming design for large-scale antenna arrays," *IEEE J. Sel. Top. Signal Process.*, vol. 10, no. 3, pp. 501–513, 2016.
- [51] T. Wei, L. Wu, K. V. Mishra, and M. B. Shankar, "Multiple IRS-assisted wideband dual-function radar-communication," in *Proc. 2nd IEEE Int. Symp. on Joint Commun. & Sensing (JC&S)*, pp. 1–5, IEEE, 2022.
- [52] P. Commware, "Holographic beamforming and phased arrays," Kirkland, WA, 2019.
- [53] A. Aubry, A. De Maio, and M. M. Naghsh, "Optimizing radar waveform and Doppler filter bank via generalized fractional programming," *IEEE J. Sel. Top. Signal Process.*, vol. 9, no. 8, pp. 1387–1399, 2015.



Pavan Kumar Gadamsetty (Student Member, IEEE) received the B.E. degree in Electronics and Communication engineering from Andhra University, Visakhapatnam, India, in 2011, the M.Tech. degree in Electrical engineering from the Indian Institute of Technology (IIT), Kanpur, in 2014. From August 2014 to December 2018, he worked at Cisco Systems, Bangalore, India. He is currently pursuing a Ph.D. degree in Electrical Communication engineering from the Indian Institute of Science, Bangalore. His current research interest includes channel estimation techniques, precoding techniques for massive MIMO systems, and emerging technologies like RIS and RHS in wireless communications.



K V S HARI (Fellow, IEEE) is a Professor in the Department of ECE, and Director, Centre for Brain Research, Indian Institute of Science (IISc), Bangalore. He holds a PhD (Systems Science) from U C San Diego and has been a visiting faculty at Stanford University and Affiliate Professor at KTH-Royal Institute of Technology, Stockholm. His research interests are in Signal Processing and Deep Learning with applications to 5G wireless communications, indoor positioning, dual function radar and communication systems, autonomous navigation, neuroscience, and affordable MRI systems. He is a co-author of the IEEE 802.16 standard on wireless channel models and also served as Chair, Standardisation Committee, Telecom Standards Development Society, India. He was leading the British Telecom India Research Centre (BTIRC) at IISc. He was an Editor of EURASIP's Signal Processing and is currently the Editor-in-Chief (Electrical Sciences) of *Sadhana*, the journal of the Indian Academy of Sciences published by Springer. He is a Fellow of the Indian National Academy of Engineering, Indian National Science Academy and IEEE. He was on the Board of Governors, IEEE Signal Processing Society as VP-Membership. More details at <http://ece.iisc.ac.in/~hari>.



Lajos Hanzo is a Fellow of the Royal Academy of Engineering, FIEEE, FIET, Fellow of EURASIP and a Foreign Member of the Hungarian Academy of Sciences. He coauthored 2000+ contributions at IEEE Xplore and 19 Wiley-IEEE Press monographs. He was bestowed upon the IEEE Eric Sumner Technical Field Award. More details at (<http://www-mobile.eecs.soton.ac.uk>, https://en.wikipedia.org/wiki/Lajos_Hanzo)